

Cross Sections for the $\gamma p \rightarrow K^{*0}\Sigma^+$ Reaction at $E_\gamma = 1.7 - 3.0$ GeV

I. Hleiqawi,¹ K. Hicks,¹ D.S. Carman,^{1,32} T. Mibe,¹ G. Niculescu,²⁰ A. Tkabladze,¹³ M. Amarian,²⁶
 P. Ambrozewicz,¹¹ M. Anghinolfi,¹⁷ G. Asryan,³⁷ H. Avakian,³² H. Bagdasaryan,²⁶ N. Baillie,³⁶ J.P. Ball,²
 N.A. Baltzell,³¹ V. Batourine,²¹ M. Battaglieri,¹⁷ K. Beard,²⁰ I. Bedlinskiy,¹⁹ M. Bellis,⁴ N. Benmouna,¹³
 B.L. Berman,¹³ A.S. Biselli,⁴ S. Bouchigny,¹⁸ S. Boiarinov,³² R. Bradford,^{4,*} D. Branford,¹⁰ W.J. Briscoe,¹³
 W.K. Brooks,³² S. Bültmann,²⁶ V.D. Burkert,³² C. Butuceanu,^{36,†} J.R. Calarco,²⁴ S.L. Careccia,²⁶ B. Carnahan,⁶
 S. Chen,¹² P.L. Cole,¹⁵ P. Collins,² P. Coltharp,¹² D. Crabb,³⁵ H. Crannell,⁶ V. Crede,¹² J.P. Cummings,²⁷
 R. De Masi,⁷ R. De Vita,¹⁷ E. De Sanctis,¹⁶ P.V. Degtyarenko,³² L. Dennis,¹² A. Deur,³² C. Djalali,³¹ R. Dickson,⁴
 G.E. Dodge,²⁶ J. Donnelly,¹⁴ D. Doughty,^{8,32} M. Dugger,² S. Dytman,²⁹ O.P. Dzyubak,³¹ H. Egiyan,^{32,‡}
 K.S. Egiyan,³⁷ L. Elouadrhiri,³² P. Eugenio,¹² G. Fedotov,²³ G. Feldman,¹³ R. Fersch,³⁶ R. Feuerbach,⁴
 M. Garçon,⁷ G. Gavalian,^{26,‡} G.P. Gilfoyle,³⁰ K.L. Giovanetti,²⁰ F.X. Girod,⁷ J.T. Goetz,³ A. Gonenc,¹¹
 R.W. Gothe,³¹ K.A. Griffioen,³⁶ M. Guidal,¹⁸ N. Guler,²⁶ L. Guo,³² V. Gyurjyan,³² R.S. Hakobyan,⁶ J. Hardie,^{8,32}
 D. Heddle,⁸ F.W. Hersman,²⁴ M. Holtrop,²⁴ C.E. Hyde-Wright,²⁶ Y. Ilieva,¹³ D.G. Ireland,¹⁴ B.S. Ishkhanov,²³
 M.M. Ito,³² D. Jenkins,³⁴ H.S. Jo,¹⁸ K. Joo,⁹ H.G. Juengst,²⁶ N. Kalantarians,²⁶ J.D. Kellie,¹⁴ M. Khandaker,²⁵
 K. Kim,²¹ W. Kim,²¹ A. Klein,²⁶ F.J. Klein,⁶ A.V. Klimenko,²⁶ M. Kossov,¹⁹ Z. Krahn,⁴ L.H. Kramer,^{11,32}
 V. Kubarovskiy,²⁷ J. Kuhn,⁴ S.E. Kuhn,²⁶ S.V. Kuleshov,¹⁹ J. Lachniet,²⁶ J.M. Laget,^{32,§} J. Langheinrich,³¹
 D. Lawrence,²² J. Li,²⁷ K. Livingston,¹⁴ H. Lu,³¹ K. Lukashin,³² M. MacCormick,¹⁸ S. McAleer,¹² B. McKinnon,¹⁴
 J. McNabb,⁴ B.A. Mecking,³² M.D. Mestayer,³² C.A. Meyer,⁴ K. Mikhailov,¹⁹ R. Minehart,³⁵ M. Mirazita,¹⁶
 R. Miskimen,²² V. Mokeev,²³ K. Moriya,⁴ S.A. Morrow,^{7,18} M. Moteabbed,¹¹ G.S. Mutchler,²⁸ E. Munevar,¹³
 P. Nadel-Turonski,¹³ R. Nasseripour,³¹ S. Niccolai,¹⁸ I. Niculescu,²⁰ B.B. Niczyporuk,³² M.R. Niroula,²⁶
 R.A. Niyazov,³² M. Nozar,³² M. Osipenko,^{17,23} A.I. Ostrovidov,¹² K. Park,²¹ E. Pasyuk,² C. Paterson,¹⁴
 J. Pierce,³⁵ N. Pivnyuk,¹⁹ O. Pogorelko,¹⁹ S. Pozdniakov,¹⁹ B. Preedom,³¹ J.W. Price,^{5,¶} Y. Prok,^{35,**}
 D. Protopopescu,¹⁴ B.A. Raue,^{11,32} G. Riccardi,¹² G. Ricco,¹⁷ M. Ripani,¹⁷ B.G. Ritchie,² F. Ronchetti,¹⁶
 G. Rosner,¹⁴ P. Rossi,¹⁶ F. Sabatié,⁷ C. Salgado,²⁵ J.P. Santoro,^{34,32,††} V. Sapunenko,³² R.A. Schumacher,⁴
 V.S. Serov,¹⁹ Y.G. Sharabian,³² E.S. Smith,³² L.C. Smith,³⁵ D.I. Sober,⁶ A. Stavinsky,¹⁹ S.S. Stepanyan,²¹
 S. Stepanyan,³² B.E. Stokes,¹² P. Stoler,²⁷ I.I. Strakovsky,¹³ S. Strauch,³¹ M. Taiuti,¹⁷ S. Taylor,¹
 D.J. Tedeschi,³¹ U. Thoma,^{32,‡‡} R. Thompson,²⁹ L. Todor,⁴ S. Tkachenko,²⁶ C. Tur,³¹ M. Ungaro,⁹
 M.F. Vineyard,³³ A.V. Vlassov,¹⁹ K. Wang,³⁵ L.B. Weinstein,²⁶ D.P. Weygand,³² S. Whisnant,²⁰ M. Williams,⁴
 E. Wolin,³² M.H. Wood,^{31,§§} A. Yegneswaran,³² L. Zana,²⁴ J. Zhang,²⁶ B. Zhao,⁹ and Z. Zhao³¹

(The CLAS Collaboration)

¹Ohio University, Athens, Ohio 45701

²Arizona State University, Tempe, Arizona 85287-1504

³University of California at Los Angeles, Los Angeles, California 90095-1547

⁴Carnegie Mellon University, Pittsburgh, Pennsylvania 15213

⁵California State University, Dominguez Hills, Carson, CA 90747

⁶Catholic University of America, Washington, D.C. 20064

⁷CEA-Saclay, Service de Physique Nucléaire, F91191 Gif-sur-Yvette, France

⁸Christopher Newport University, Newport News, Virginia 23606

⁹University of Connecticut, Storrs, Connecticut 06269

¹⁰Edinburgh University, Edinburgh EH9 3JZ, United Kingdom

¹¹Florida International University, Miami, Florida 33199

¹²Florida State University, Tallahassee, Florida 32306

¹³The George Washington University, Washington, DC 20052

¹⁴University of Glasgow, Glasgow G12 8QQ, United Kingdom

¹⁵Idaho State University, Pocatello, Idaho 83209

¹⁶INFN, Laboratori Nazionali di Frascati, 00044 Frascati, Italy

¹⁷INFN, Sezione di Genova, 16146 Genova, Italy

¹⁸Institut de Physique Nucleaire ORSAY, Orsay, France

¹⁹Institute of Theoretical and Experimental Physics, Moscow, 117259, Russia

²⁰James Madison University, Harrisonburg, Virginia 22807

²¹Kyungpook National University, Daegu 702-701, South Korea

²²University of Massachusetts, Amherst, Massachusetts 01003

²³Moscow State University, General Nuclear Physics Institute, 119899 Moscow, Russia

²⁴University of New Hampshire, Durham, New Hampshire 03824-3568

²⁵Norfolk State University, Norfolk, Virginia 23504

²⁶Old Dominion University, Norfolk, Virginia 23529

²⁷Rensselaer Polytechnic Institute, Troy, New York 12180-3590

²⁸Rice University, Houston, Texas 77005-1892

²⁹University of Pittsburgh, Pittsburgh, Pennsylvania 15260

³⁰University of Richmond, Richmond, Virginia 23173

³¹University of South Carolina, Columbia, South Carolina 29208

³²Thomas Jefferson National Accelerator Facility, Newport News, Virginia 23606

³³Union College, Schenectady, NY 12308

³⁴Virginia Polytechnic Institute and State University, Blacksburg, Virginia 24061-0435

³⁵University of Virginia, Charlottesville, Virginia 22901

³⁶College of William and Mary, Williamsburg, Virginia 23187-8795

³⁷Yerevan Physics Institute, 375036 Yerevan, Armenia

(Dated: May 24, 2018)

Differential cross sections for the reaction $\gamma p \rightarrow K^{*0}\Sigma^+$ are presented in photon energy range from 1.7 to 3.0 GeV. The K^{*0} was detected by its decay products, $K^+\pi^-$, in the CLAS detector at Jefferson Lab. These data are the first K^{*0} photoproduction cross sections ever published over a broad range of angles. Comparison with a theoretical model based on the vector and tensor K^* -quark couplings shows good agreement with the data, except at forward angles, suggesting that the role of scalar κ meson exchange should be investigated.

PACS numbers: 13.60.-r,13.60.Le,13.60.Rj,14.40.Ev

I. INTRODUCTION

The photoproduction of the vector meson K^* has some advantages over its non-strange partners, the ρ and ω , in probing the dynamics usually included in theoretical calculations. Because the K^* has non-zero strangeness, pomeron exchange is not possible. In comparison, t -channel pomeron exchange dominates the total cross section for ρ , ω and ϕ photoproduction at high energy. Near threshold energies, scalar meson exchange in the t -channel contributes strongly to ρ and ω photoproduction, but the equivalent diagram for K^* photoproduction, via scalar κ exchange, has not been established. The $\kappa(800)$ was omitted [22] from the Particle Data Group [1] primary tables because the existence of this state is controversial. Instead, K^* photoproduction models use t -channel kaon exchange, constrained by KN scattering and kaon photoproduction data. Since this is the dominant term at forward angles, the t -channel parameters in theoretical models are already known. However, the lack

of K^* photoproduction data in the past has prevented further theoretical development. In particular, the need for possible κ exchange is uncertain.

We present here the first data for $K^{*0}\Sigma^+$ photoproduction from the proton over a wide angular range for photon energies near threshold ($E_\gamma = 1.7 - 3.0$ GeV). Because of the short lifetime of $K^{*0} \rightarrow K^+\pi^-$, a detector with large acceptance is needed to capture the decay particles. Here, we use the CLAS detector [2] where multiple particles can be detected with reasonable efficiency.

In addition to investigating the t -channel, as described above, our data will be compared with a theoretical model to extract information on the vector and tensor coupling strength of the K^{*0} to quarks in s -channel nucleon resonances. Nucleon resonances are predicted to have significant branching ratios to kaons and, if the mass is high enough, to K^* channels [3]. The overlap between the quark wave functions, as predicted in theoretical models, and the branching ratio for nucleon resonances decaying to K^*Y , can be calculated using an effective theory as described below. Comparison of K^* production data with these calculations provides feedback for models of nucleon resonances.

In the theoretical description of $\gamma N \rightarrow K^*Y$ reactions, where Y denotes a hyperon, a simplification occurs for neutral K^{*0} production, where K^{*0} exchange in the t -channel is strongly suppressed [4] (it requires a higher multipolarity than the dominant $M1$ transition). Also there is no seagull diagram, since this term is directly proportional to the charge of the vector meson. Hence, there are some theoretical simplifications when studying K^{*0} photoproduction compared with K^{*+} production.

Calculations are available based on a quark model description of the meson-hyperon vertex in the s and u channels [4]. In this model there are only two free parameters corresponding to the vector and tensor couplings, which are common to all intermediate states (N^* or Y^*) and depend only on the quark mass. Using this approach,

*Current address:Rochester University, Rochester, New York 14627

†Current address:University of Regina, Regina Saskatchewan, Canada S4S 0A2

‡Current address:University of New Hampshire, Durham, New Hampshire 03824-3568

§Current address:CEA-Saclay, Service de Physique Nucléaire, F91191 Gif-sur-Yvette,Cedex, France

¶Current address:University of California at Los Angeles, Los Angeles, California 90095-1547

**Current address:Massachusetts Institute of Technology, Cambridge, Massachusetts 02139-4307

††Current address:Catholic University of America, Washington, D.C. 20064

‡‡Current address:Physikalisches Institut der Universitaet Giessen, 35392 Giessen, Germany

§§Current address:University of Massachusetts, Amherst, Massachusetts 01003

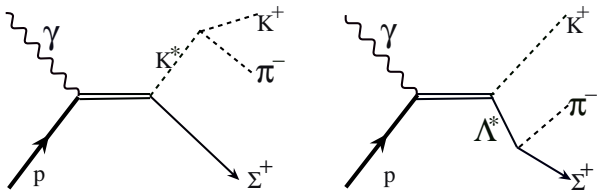


FIG. 1: Schematic diagrams showing K^{*0} (left) and Y^* (right) production. Both diagrams lead to the same final state.

a consistent picture of both K^* and non-strange vector meson production can be developed. In Ref. [4], the cross sections for K^* production were predicted based on SU(3) symmetry and quark coupling parameters extracted from ω photoproduction data. The current data will be compared with this theoretical model.

In contrast to the theoretical advantages of K^{*0} photoproduction, there are some experimental challenges to be met. The cross sections are small, in part due to the larger mass of the K^* , which suppresses production compared to that of lighter mesons. Also, the multiparticle final state requires large acceptance detectors rather than traditional magnetic spectrometers with small solid angle acceptances. Perhaps for this reason, there is only one experiment reported in the literature for K^* photoproduction [5], using 20-70 GeV photons (well above threshold). More troublesome is the physics background from production of Y^* hyperon resonances which decay to $Y\pi$ final states; these reactions have overlapping kinematics with K^* production and must be subtracted in the analysis. An example of two diagrams having the same final state is shown in Fig. 1. As discussed below, a Dalitz plot of the invariant mass of the $K\pi$ system versus that of the $Y\pi$ system (not shown) has horizontal and vertical bands for K^* and Y^* resonances, respectively. The bands will cross where the kinematics overlap, at which point these reactions are indistinguishable. As described in Section III, care must be taken to extract the K^{*0} cross sections independently from the Y^* background.

From a broader perspective, data for (γ, K) and (γ, K^*) reactions together provide clear information about the production of an $s\bar{s}$ pair from the vacuum [4]. For example, measurements of polarization transfer in the $\bar{e}p \rightarrow e'K^+\bar{\Lambda}$ reaction [6] have shown that the $s\bar{s}$ are produced with spins primarily anti-aligned. In contrast, similar measurements with the spin-1 K^* are expected to produce the $s\bar{s}$ pair with spins aligned. A coherent description of both reactions will likely be needed in order to do a full coupled-channel analysis, since K^* exchange contributes to t -channel diagrams in kaon production, and kaon exchange contributes to t -channel diagrams in K^* production [7].

II. EXPERIMENTAL DETAILS

The experiment was carried out in Hall B of the Thomas Jefferson National Accelerator Facility, using the CLAS detector [2]. An electron beam of energy 3.115 GeV was incident on a gold foil, creating a bremsstrahlung photon beam. Each photon was tagged by measuring the energy of the electron in a tagging spectrometer [8], with an upper range at 95% of the incident electron energy. The photons then passed through a collimator before reaching an 18.0 cm long liquid-hydrogen target in the center of CLAS. The target was surrounded by a segmented scintillator, called the start counter [9].

The momentum of charged particles was determined from tracks in the drift chambers [10], located outside of the start counter. CLAS has a toroidal magnetic field [2], which was set at 50% of the maximum and oriented so that negatively charged particles bent inward toward the beam line. The outer layer of the drift chambers surrounds the region of strongest magnetic field. The time-of-flight (TOF) of particles was measured between the stop time from scintillators outside the drift chambers [11] and the start counter time. A combination of the momentum (from the drift chambers) and the TOF (from the scintillators) was used to calculate the mass of each particle. A coincidence between the tagger, the start counter and a TOF scintillator provided the event trigger.

We used the $\Delta\beta$ method for particle identification, where the measured velocity (from the TOF) is subtracted from the velocity calculated from the momentum for a given mass, and values of $|\beta_{TOF} - \beta_{calc}| < 0.1$ were accepted. The particle vertex time is calculated from the TOF for a given mass (of the kaon or pion) along with the momentum measured by the drift chambers. The particle vertex time is required to be within 1.0 ns of the photon time, measured by the tagger and extrapolated to the vertex. In addition, our analysis required both a positive kaon and a negative pion to be identified in coincidence, which suppressed accidental coincidences considerably. The same analysis steps were used for both data and Monte Carlo simulations, so particle misidentification due to kaon decays could be accounted for.

The measurement of the photon flux has been described previously [12]. Briefly, the main idea is to first count the number of “good” electrons in the tagging spectrometer, given by a timing coincidence of scintillators at the tagger focal plane, and comparing this with the number of counts in a total absorption counter (four blocks of lead glass) placed directly in the photon beam during low-intensity calibration measurements. Recoiling electrons both in and out of a coincidence window were monitored and used to calculate the rate of photons produced at the tagger. The tagger was upstream of the target, so this rate was corrected for loss of photons in the beamline between the tagger and the physics target. The rate of photons striking the target was scaled by the experimental livetime.

Monte Carlo simulations of the detector were carried

out using the software package GEANT [13], input with the detector configuration of CLAS. Detector acceptance factors obtained from simulations have been shown previously to reproduce the world data on known reactions [14]. Two event generators were used. One has a uniform distribution in two-body phase space for $K^{*0}\Sigma^+$ production, and the other has angular distributions calculated from the model of Zhao [4] for our reaction. The detector acceptances obtained using these event generators were then used to calculate the cross sections, and systematic uncertainties in the acceptance factor were estimated by comparing the two results. The average acceptance for K^{*0} detection in CLAS was about 3% and ranges from 1-6% depending on the photon beam energy and the K^{*0} angle. Details are given in Ref. [15].

III. DATA ANALYSIS

Events were scanned for K^+ and π^- candidates, based on the particle identification method described in the previous section. Both particles were extrapolated in time to the target vertex and were required to be within 1.0 ns of the photon time. The time resolution of the TOF system, σ_t , is about 100-300 ps, depending on the location in the CLAS detector. A time cut of $\pm 3\sigma_t$ was used for each particle. The time resolution in the Monte Carlo simulation is well matched with that seen by our experiment, so the loss of particles (for example due to K^+ decay) outside of the timing cuts is folded into the detector acceptance calculation.

After identifying a valid K^+ and π^- , the missing mass for the $\gamma p \rightarrow K^+\pi^-X$ reaction, $MM(K^+\pi^-)$, was calculated, as shown by Fig. 2(a). The Σ^+ peak dominates the spectrum, at a mass of 1.189 GeV/ c^2 , riding on a smooth background. Next, the invariant mass of the system, $M(K^+\pi^-)$ is calculated. After requiring events in the Σ^+ region, $1.175 < MM(K^+\pi^-) < 1.205$ GeV/ c^2 , the invariant mass spectrum is shown in Fig. 2(b). The K^{*0} peak is visible at a mass of 0.896 GeV/ c^2 , which has an intrinsic width of about 0.05 GeV/ c^2 . The K^{*0} peak sits on top of background due to competing processes, such as Y^* production (see Fig. 1). The non- Y^* background can be removed by the sideband subtraction method. Events in regions of $MM(K^+\pi^-)$ on either side of the Σ^+ region, inside the vertical lines in Fig. 2(a), are plotted by the dashed and dotted lines in Fig. 2(b).

Background from $\Sigma(1385)$, $\Lambda(1405)$ and $\Lambda(1520)$ resonances were calculated by simulations with angular distributions described by an exponential t -slope [16], which are then projected onto the $M(K^+\pi^-)$ mass. The strength of each Y^* resonance is treated as a free parameter in the fits to each kinematic bin (see below). Interference between Y^* resonances and K^{*0} production were studied and found to be small [15], keeping the cross sections within the systematic uncertainties.

The data were processed in 6 angular bins for each of 9 photon energy bins. The variable for the angular

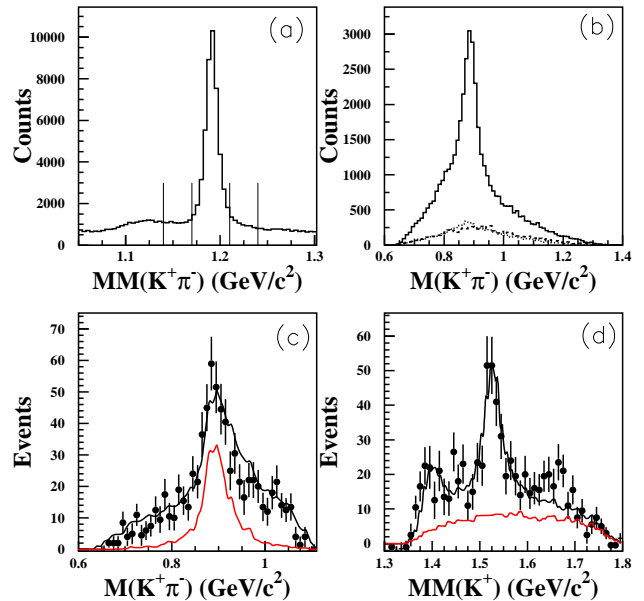


FIG. 2: (Color online) (a) Missing mass for the $\gamma p \rightarrow K^+\pi^-X$ reaction summed over all angles and photon energies. (b) Invariant mass of the $K^+\pi^-$ system, with the same event selection, for events in the Σ^+ peak (solid) and the sideband regions (dashed and dotted) shown in (a). (c) $M(K^+\pi^-)$ for $E_\gamma = 2.24$ - 2.36 GeV and $-0.2 < \cos\theta_{K^*} < 0.1$ showing the full fit (black) and the K^{*0} peak component (red). (d) $MM(K^+)$ showing the $\Lambda(1520)$ and other hyperon peaks (see Fig. 1, right) along with the curves as in (c).

bins was $\cos\theta_{K^*}$ (where θ_{K^*} is the angle of the K^{*0} in the center of mass system). Fewer counts were found at backward angles, and so the bin sizes were made larger for $\cos\theta_{K^*} < 0$. Note that our angular coverage stops at $\cos\theta_{K^*} = 0.9$. Beyond this point, the detector acceptance falls off sharply. The photon energy bins span the range from 1.71 GeV up to 2.96 GeV. The photon energy bins are not equally spaced in order to avoid regions where tagger counters were not working properly.

Yields in each bin were extracted by fitting the K^{*0} peak, which rides on a nonlinear background. The background due to sidebands of the Σ^+ peak were subtracted in each bin. The remaining background was fit directly to the shape of Monte Carlo simulations by adjusting the relative magnitudes of 3-body phase space (K^+, π^-, Σ^+) and K^+Y^* event generators, where Y^* represents the $\Sigma(1385)$, $\Lambda(1405)$ and $\Lambda(1520)$ resonances. A sample result of the template fits is shown in parts (c) and (d) of Fig. 2 for a single kinematic bin. The strengths of the Y^* resonances were constrained by simultaneous fits to the missing mass spectra of the kaon, $MM(K^+)$, for each bin. The shape of the K^{*0} peak was fixed to the shape from the GEANT simulations, which used a Breit-Wigner parameterization for the known K^{*0} resonance mass and width. The reduced χ^2 of the fits was typically between 1.0 to 2.5. When the fit is restricted to the regions surrounding the K^{*0} peak and low-lying Y^* res-

onances, then values of χ^2 near unity are obtained. This suggests that higher mass resonances, like the $\Lambda(1660)$, could improve the overall simulation of the data. However, the fits indicate that the addition of more Y^* resonances will not change the cross sections outside of the systematic uncertainty range given below.

As a measure of the systematic uncertainty of the fitting procedure, we varied several event selection parameters and refit the K^{*0} peak. For example, we varied the width of the mass cut on the Σ^+ peak, and the corresponding sideband regions. Also, we tried the fits with and without the $\Lambda(1405)$ resonance, which has nearly overlapping kinematics with the $\Sigma(1385)$ resonance. After comparing the fits for variations in the analysis procedures, we determined that the uncertainty in the K^{*0} yield is $\pm 18\%$.

The cross section in each kinematic bin depends on the detector acceptance. The CLAS detector has been modeled using the software package GEANT, as described above, using two different event generators. Because of the large bins in angle, which were necessary due to the limited statistics in the K^{*0} peaks, there was not much difference between acceptances calculated using each event generator. Hence, we chose the flat phase-space model for the detector acceptance corrections rather than the one based on Ref. [4]. The branching ratio of $K^{*0} \rightarrow K^+\pi^-$ has been accounted for.

The systematic uncertainty in the yield extraction, as described above was 18%. Other systematic uncertainties were calculated from varying the cuts used for particle identification (8%), varying the allowed fiducial region for the particles detected in CLAS (8%), the dependence on the Monte Carlo event generator (4%) and the luminosity normalization (7%). Added in quadrature, the total systematic uncertainty for our measurement is $\pm 23\%$.

IV. RESULTS AND DISCUSSION

The differential cross sections are presented in Fig. 3 for nine photon energy bins. Also shown are curves calculated from the model of Zhao [4] using the parameters $a = -2.2$ and $b = 0.80$ for the vector and tensor K^* -quark couplings, respectively. These parameters are different than those given in Ref. [4], $a = -2.8$ and $b = -5.9$, which were extrapolated from ω production data using SU(3) symmetry. The current values, which were fitted to the K^{*0} data, are significantly smaller than those predicted in Ref. [4], however it is worth noting that some corrections were made to the computer code used in Ref. [4], so the parameters a and b used in that reference should be reexamined. The first photon energy bin was not fit because of numerical instability of the calculation close to threshold.

Near threshold, the data have a fairly flat angular distribution. As the energy increases, the forward and backward angles dominate, showing substantial t -channel and u -channel contributions. The u -channel is implicitly in-

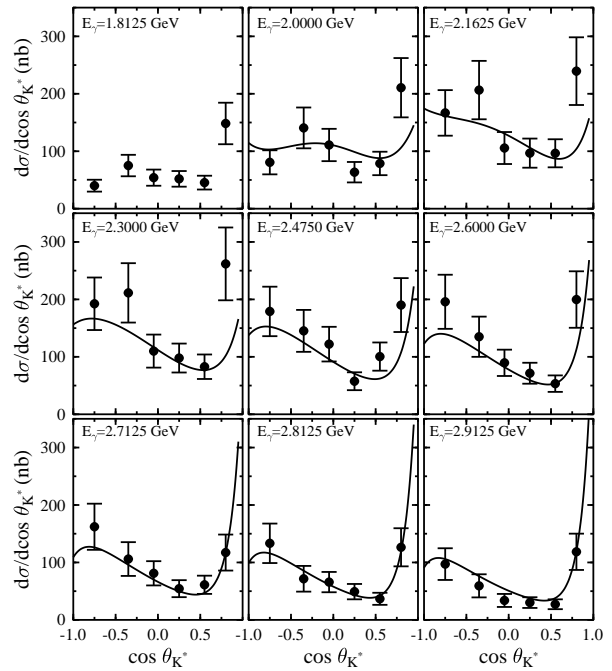


FIG. 3: Cross sections for the reaction $\gamma p \rightarrow K^{*0}\Sigma^+$ as a function of angle for the energy bins shown. The curves are from the model of Zhao [4] using vector and tensor couplings adjusted to give the best fit to the data. Error bars include systematic uncertainties. For numbers, see Ref. [18].

cluded in the K^* -quark couplings (parameters a and b above) which also control the s -channel amplitudes. The t -channel coupling in the Zhao model is, in principle, completely determined by a single diagram with K^0 exchange, where the $KN\Sigma$ vertex coupling is taken from KN scattering and the $\gamma K^+ K^*$ electromagnetic coupling is fixed from K^* radiative decay. In other words, there should be no free parameters in the t -channel for this model. However, in order to obtain better agreement with the data at forward angles, the t -channel amplitude was multiplied by a factor of 0.8. This factor is perhaps justified because there may be other t -channel diagrams that can contribute, such as scalar κ exchange, that are not included in the Zhao model.

The energy dependence of the cross sections is presented in Fig. 4 for the six angle bins shown. The solid curves use the same parameters (a and b) as given above. The good agreement between theory and experiment suggests that the K^* -quark dynamics used in the Zhao model are reasonable. The only serious discrepancy is for the most forward angle bin, where the global fit underpredicts the cross section at lower photon energies. Clearly, the energy dependence of the t -channel strength within the context of the Zhao model is not correct to reproduce the forward angle strength. Note that if the Zhao model is fitted to this single angular bin, a reasonable fit can be obtained, but at the expense of destroying the good agreement with the data at larger angles.

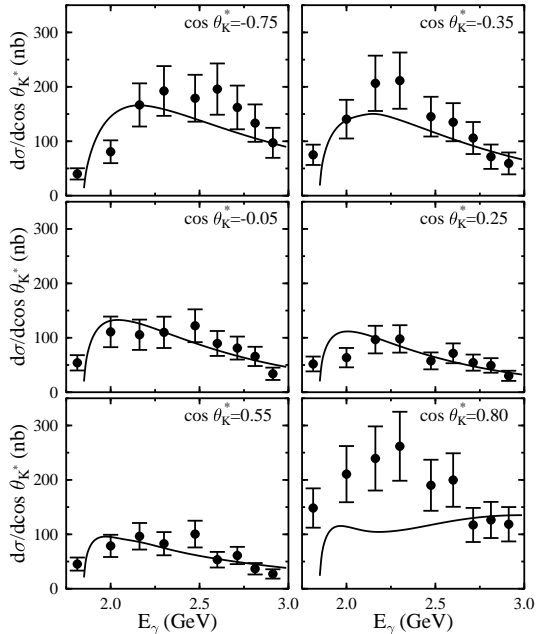


FIG. 4: Cross sections for the reaction $\gamma p \rightarrow K^{*0}\Sigma^+$ as a function of energy for the angular bins shown. The curves are from the same model as in the previous figure. Error bars include systematic uncertainties.

V. CONCLUSIONS

Using the CLAS detector, the first near-threshold measurement of K^{*0} photoproduction cross sections has been obtained. The results reported here show that the angular distributions are forward peaked, as expected from t -channel diagrams with kaon exchange, and increase slowly at backward angles, showing the effect of s - and u -channel resonances that couple to $K^{*0}\Sigma^+$. As a function of energy, the cross sections exhibit a maximum just above threshold and then a smooth decrease.

The data are in good agreement with the Zhao model,

which uses a K^* -quark coupling with only two constant parameters, except at the most forward angle bin. The forward angles are dominated by the t -channel, where K^0 exchange is expected to have the largest amplitude. By tuning the model parameters, in a global fit to the data, the calculations reproduce the general trend of the data at larger angles. The other aspects of this model are constrained by previous data or predicted from resonance properties from quark models. The lack of agreement for the energy dependence of the t -channel could indicate that other diagrams, like scalar κ exchange, need to be investigated.

Improvements in the statistics will enable smaller kinematic bins, which in turn will further constrain comparison with theoretical models. In addition, photoproduction of $K^{*+}\Lambda$ will provide new information, and simultaneous comparisons of theoretical models to both K^{*+} and K^{*0} reactions, which have different t -channel dependences, will shed light on the role of scalar κ exchange [17]. Due to parity and angular momentum conservation, the κ cannot contribute to conventional kaon photoproduction, so data on K^*Y reactions is perhaps the best way to investigate the possibility of κ exchange. Preliminary data on K^{*+} are already available [19] and larger data sets from CLAS are being analyzed [20, 21].

Special thanks go to Q. Zhao and C. Bennhold for discussions and access to their computer code. Event generators for the Y^* states are from L. Guo and G. Mutchler. We acknowledge the outstanding efforts of the staff of the Accelerator and Physics Divisions at Jefferson Lab who made this experiment possible. This work was supported in part by the U.S. Department of Energy, the National Science Foundation, the Istituto Nazionale di Fisica Nucleare, the French Centre National de la Recherche Scientifique and Commissariat à l’Energie Atomique, and the Korea Science and Engineering Foundation. Jefferson Science Associates (JSA) operates the Thomas Jefferson National Accelerator Facility for the U.S. Department of Energy under contract DE-AC05-06OR23177.

-
- [1] Particle Data Group, *Review of Particle Properties*, Phys. Lett. B **592**, 644 (2004).
 - [2] B. Mecking *et al.*, Nucl. Instr. Meth. **A503**, 513 (2003).
 - [3] S. Capstick and W. Roberts, Phys. Rev. D **58**, 074011 (1998).
 - [4] Q. Zhao, J.S. Al-Khalili, and C. Bennhold, Phys. Rev. C **64**, 052201 (2001).
 - [5] M. Atkinson *et al.*, Z. Phys. **C30**, 521 (1986).
 - [6] D.S. Carman *et al.*, Phys. Rev. Lett. **90**, 131804 (2003).
 - [7] B. Juliá-Díaz, B. Saghai, T.-S. H. Lee and F. Tabakin, Phys. Rev. C **73**, 055204 (2006).
 - [8] D.L. Sober *et al.*, Nucl. Instr. Meth. **A440**, 263 (2000).
 - [9] S. Taylor *et al.*, Nucl. Instr. Meth. **A462**, 484 (2001).
 - [10] M.D. Mestayer *et al.*, Nucl. Instr. Meth. **A449**, 81 (2000).
 - [11] E.S. Smith *et al.*, Nucl. Instr. Meth. **A432**, 265 (1999).
 - [12] J. Ball and E. Pasyuk, CLAS Note 2005-002, <http://www.jlab.org/Hall-B/clas/index.cfm>.
 - [13] CERN Program Library Long Writeup W5013 (1993).
 - [14] J.W. McNabb *et al.*, Phys. Rev. C **69**, 042201 (2004).
 - [15] I. Hleiqawi, Ph.D. thesis, Ohio University, 2006; K. Hicks and T. Mibe, CLAS Analysis Note <http://www.jlab.org/~hicks/kstar-note.pdf>.
 - [16] S. Barrow *et al.*, Phys. Rev. C **64**, 044601 (2001).
 - [17] Y. Oh and H. Kim, hep-ph/0605105.
 - [18] I. Hleiqawi *et al.*, nucl-ex/0701036.
 - [19] L. Guo and D.P. Weygand, hep-ex/0601010.
 - [20] K. Hicks and S. Stepanyan, Jefferson Lab Experiment E03-113.
 - [21] M. Battaglieri *et al.*, Jefferson Lab Experiment E04-017.
 - [22] See the notes on scalar mesons in the Meson Particle Listings for $f_0(600)$ in Ref. [1].

TABLE I: Cross sections, with total uncertainties, in each bin for the $\gamma p \rightarrow K^* \Sigma^+$ reaction.

Energy bin (GeV)		Cross section (nb) for each kinematic bin						
E_γ	ΔE_γ	$\cos\theta_{K^*}$	-0.75	-0.35	-0.05	0.25	0.55	0.8
		$\Delta\cos\theta_{K^*}$	0.5	0.3	0.3	0.3	0.3	0.2
1.8125	0.2000		40.1±10.3	75.1±18.7	54.0±14.1	51.9±13.6	45.4±12.0	148.3±36.1
2.0000	0.1750		80.7±21.0	140.6±35.5	110.9±28.1	63.5±17.8	78.7±20.4	210.6±51.6
2.1625	0.1500		166.7±39.7	206.4±50.8	105.6±27.8	96.7±25.4	96.4±24.4	239.4±58.9
2.3000	0.1250		192.3±45.7	211.4±51.7	110.0±28.8	97.9±25.2	82.8±21.3	261.8±63.4
2.4750	0.1250		179.0±43.1	145.2±36.5	122.1±30.2	57.5±15.6	100.5±24.6	190.1±46.9
2.6000	0.1350		195.8±47.1	135.0±35.0	89.6±22.9	71.5±18.2	53.3±14.3	199.7±49.2
2.7125	0.1000		162.1±40.2	105.9±29.4	81.1±21.1	54.4±14.8	61.1±15.9	117.2±31.3
2.8125	0.1000		133.3±34.4	71.6±22.4	65.8±17.7	49.2±13.4	36.7±10.5	126.4±33.1
2.9125	0.1000		97.1±27.6	59.3±20.1	33.9±11.3	30.1±9.3	27.2±8.6	118.5±31.6

